Nanoscale

ROYAL SOCIETY OF CHEMISTRY

PAPER

View Article Online
View Journal | View Issue

Cite this: *Nanoscale*, 2025, **17**, 888

Metal oxide plating for maximizing the performance of ruthenium(IV) oxide-catalyzed electrochemical oxygen evolution reaction†

Shin-ichi Naya, [a] Mio Nagamitsu,[b] Hisashi Sugime, [b,c] Tetsuro Soejima [b,c] and Hiroaki Tada *[d]

Received 8th September 2024,
Accepted 14th November 2024

DOI: 10.1039/d4nr03678f

rsc.li/nanoscale

Hydrogen production by proton exchange membrane water electrolysis requires an anode with low overpotential for oxygen evolution reaction (OER) and robustness in acidic solution. While exploring new electrode materials to improve the performance and durability, optimizing the morphology of typical materials using new methods is a big challenge in materials science. RuO_2 is one of the most active and stable electrocatalysts, but further improvement in its performance and cost reduction must be achieved for practical use. Herein, we present a novel technology, named "metal oxide plating", which can provide maximum performances with minimum amount. A uniform single-crystal RuO_2 film with thickness of ~2.5 nm was synthesized by a solvothermal-post heating method at an amount (x) of only 18 μg cm^{-2} (ST-RuO_2(18)//TiO_2 NWA). OER stably proceeds on ST-RuO_2(18)//TiO_2 NWA with ~100% efficiency to provide a mass-specific activity (MSA) of 341 A g_{cat}^{-1} at 1.50 V (*vs.* RHE), exceeding the values for most of the state-of-the-art RuO_2 electrodes.

Introduction

Electrochemical (EC) water splitting can be a favorable green process for hydrogen (H_2) production.[1] The key step in water electrolysis is the oxygen evolution reaction (OER), involving proton-coupled four-electron transfer and O–O bond formation because of its large overpotential.[2] H_2 production by proton exchange membrane water electrolysis requires an anode with high electrocatalytic activity for OER and durability against electrolysis in acidic electrolytes.[3] Among various electrocatalyst materials, RuO_2 possesses the lowest overpotential for OER,[4] while only RuO_2 and IrO_2 are electronically conducting and stable at the potential where OER can occur.[5] Since these precious metal oxides are very expensive, devising a cost-saving strategy is also of great importance for practical use. The best indicator for the cost-performance of electrodes is the mass-specific activity (MSA), which is provided by the product of specific activity (SA) and specific surface area (SSA) (eqn (1)).

$$\text{MSA (A } g_{cat}^{-1}) = \text{SA (A cm}^{-2}) \times \text{SSA (cm}^2\ g_{cat}^{-1}) \quad (1)$$

Considering the relation between MSA and catalyst loading amount for the RuO_2 electrodes reported so far for OER under acidic conditions (Fig. 1 and Table S1†),[6–17] a catalyst loading amount more than ~100 μg cm^{-2} is usually necessary to obtain MSA larger than 100 A g_{cat}^{-1}. A major challenge in EC

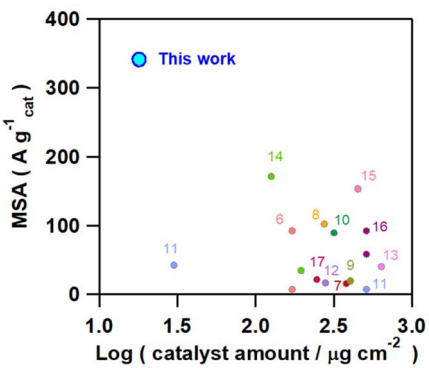

Fig. 1 Relationship between mass-specific activity (MSA) and catalyst-loading amount (circles) of the RuO_2 electrodes reported so far for OER under acidic conditions. Blue circle expresses the data of the present study. The number expresses the reference numbers in the text.

[a]*Environmental Research Laboratory, Kindai University, 3-4-1, Kowakae, Higashi-Osaka, Osaka 577-8502, Japan. E-mail: shinichi.naya@itp.kindai.ac.jp*
[b]*Graduate School of Science and Engineering, Kindai University, 3-4-1, Kowakae, Higashi-Osaka, Osaka 577-8502, Japan*
[c]*Department of Applied Chemistry, Faculty of Science and Engineering, Kindai University, 3-4-1, Kowakae, Higashi-Oaka, Osaka 577-8502, Japan*
[d]*Institutes of Innovation for Future Society, Nagoya University, Furo-cho, Chikusa-ku, Nagoya, Aichi 464-8603, Japan. E-mail: htada0409@gmail.com*
†Electronic supplementary information (ESI) available. See DOI: https://doi.org/10.1039/d4nr03678f

water splitting is to enhance the MSA by increasing the SA and SSA. Many recent studies have focused on the enhancement of the SA through a reduction in the overpotential of RuO_2 for OER by modifications, including doping,[10,13,16,18,19] hybridization with other metals,[11,20] and metal oxides,[8,14,17,21] and synthesis of multiple oxides.[21–23] On the other hand, even if unmodified RuO_2 is used as the catalyst, its MSA varies over a wide range from 6.5 to 171 A g_{cat}^{-1}, as shown in the plots (Fig. 1). Thus, it is fundamentally important to recognize how far the MSA can be enhanced by improving the quality and optimizing the morphology of RuO_2 itself and the interface quality with the electrode or support to increase the SA and SSA. The development of three-dimensional electrodes has brought about a breakthrough in the areas of electrochemistry and photoelectrochemistry.[24] The typical TiO_2 nanowire array (NWA) is a fascinating anode for photoelectrochemical water splitting[25,26] but cannot be used as the anode for EC water splitting due to its poor electric conductivity. On the contrary, RuO_2 has a metallic conductivity of 2.84×10^4 S cm^{-1} despite being a metal oxide.[27] If uniform high-quality RuO_2 film can be formed on TiO_2 NWA, it would be a very promising anode for EC water splitting. Further, RuO_2 as well as TiO_2 have excellent stability, and the strong catalyst (RuO_2)–support (TiO_2) interaction is crucial to withstand the harsh operating conditions.[28] Recent studies on nanohybrids consisting of metals and metal oxides have indicated that the morphology of deposits on a substrate can be widely tuned through crystallographic interface control between them.[29]

Herein, we show that ultrathin single-crystalline RuO_2 film can be formed on TiO_2 NWA having a $(110)_{RuO_2}//(110)_{TiO_2}$ heteroepitaxial (HEPI) relation by a solvothermal (ST)-post heating process with the RuO_2 loading amount and morphology controlled (ST-RuO_2//TiO_2 NWA), where symbol // denotes the HEPI junction. The dependence of the activities of ST-RuO_2//TiO_2 NWAs for EC and PEC OER on the RuO_2 loading amount was studied in 0.5 M H_2SO_4 electrolyte solution. Remarkably, the ST-RuO_2//TiO_2 NWA electrode with only $x = 18$ stably generates OER current with an MSA of 341 A g_{cat}^{-1}.

Experimental

Materials

Fluorine-doped tin(IV) oxide film-coated glass (FTO, TEC7), and Nafion film (Nafion 117, thickness = 0.007 inch) were purchased from Aldrich. Titanium tetra-*n*-butoxide ($Ti(OBu)_4$ > 97.0%), hydrochloric acid (HCl, 35.0–37.0%), methyl alcohol (CH_3OH > 99.8%), ethyl alcohol (C_2H_5OH > 99.5%), sulfuric acid (H_2SO_4 > 96.0%), potassium ferricyanide ($K_3[Fe(CN)_6]$ > 99.0%), potassium hexacyanoferrate(II) trihydrate ($K_4[Fe(CN)_6]\cdot 3H_2O$ > 99.5%), and ruthenium(IV) oxide (RuO_2 > 99.9) were purchased from Kanto Chemical Co. Ruthenium(III) chloride hydrate ($RuCl_3\cdot xH_2O$ > 40% as Ru) was purchased from Tokyo Chemical Industry Co. All chemicals were used as received without further purification.

Electrode preparation

Rutile TiO_2 NWA was synthesized according to a previously reported method.[16] $Ti(OBu)_4$ (0.17 mL) was dissolved in 6 M HCl (10 mL) and stirred at room temperature (298 K) for 0.5 h. The solution was put into a Teflon-reactor (volume 25 mL) and FTO (3 pieces) was immersed into the solution. The Teflon reactor was sealed in a stainless-steel autoclave and heated at 423 K for 8 h. The resulting sample was washed with distilled water and acetone and dried *in vacuo* at room temperature.

The RuO_2//TiO_2 NWA electrodes were prepared by a solvothermal-post heating method. $RuCl_3$ (1 ~ 50 mg) was added to a mixed solution of methanol (20 mL) and water (10 mL) in a Teflon-reactor (inner volume = 50 mL) and stirred at room temperature for 0.5 h. TiO_2 NWA-grown FTO plates (2 pieces) were immersed in the solution, and the Teflon reactor was sealed in a stainless-steel autoclave. The autoclave was heated at 453 K for 6 h, and the resulting sample was washed with distilled water and acetone. After drying, the sample was calcined at 673 K for 10 h in air.

For comparison, RuO_2 NP-loaded TiO_2 NWA (RuO_2/TiO_2 NWA) electrodes were prepared by the conventional impregnation method.[18] Commercial RuO_2 was dispersed into ethanol by ultrasonic irradiation for 0.5 h. After the suspension was dropped on TiO_2 NWA and dried at 323 K, the sample was calcined at 673 K for 10 h in air.

Electrode characterization

To quantify the amount of Ru loading, RuO_2//TiO_2 NWA or RuO_2/TiO_2 NWA was immersed into 6 M HCl (10 mL) in a Teflon-reactor (volume 25 mL). The Teflon-reactor was sealed in a stainless-autoclave and heated at 473 K for 12 h. The amount of Ru dissolved into the solution was quantified by inductively-coupled plasma spectroscopy. Scanning electron microscopy (SEM) observation was carried out using a Hitachi SU8230 at an applied voltage of 20 kV. For transmission electron microscopy (TEM) observation, part of RuO_2//TiO_2NWA or RuO_2/TiO_2NWA was mechanically scraped off from the FTO substrate. TEM and high resolution-TEM images, HAADF-STEM images, and EDS mapping were obtained by means of a JEOL JEM-2100F instrument at an applied voltage of 200 kV. X-ray photoelectron spectra (XPS) were measured by means of a PHI VersaProbe 4 (ULVAC-PHI) with 15 kV and 3 mA using Al Kα as the X-ray source. The peak of C 1*s* (284.6 eV) was used for energy correction. Diffuse reflectance UV-Vis-NIR spectra were measured using $BaSO_4$ as a reference (R_∞) by a UV-2600 spectrometer (Shimadzu) with an integrating sphere unit (Shimadzu, ISR-2600Plus). The spectra were transformed to absorption spectra by the Kubelka–Munk function [$F(R_\infty) = (1 - R_\infty)^2/2R_\infty$]. X-ray diffraction (XRD) patterns were obtained at 40 kV and 100 mA using a Rigaku SmartLab X-ray diffractometer.

Electrocatalytic activity for OER

Electrochemical (EC) measurements were carried out by a two-component and three-electrochemical cell with the structure

of RuO_2//TiO_2NWA or RuO_2/TiO_2NWA (working electrode), Ag/AgCl (reference electrode)|0.5 M H_2SO_4 aqueous solution | Nafion|Pt film (counter electrode) in the dark. The active area of the working electrode was 1 cm^2 (1 cm × 1 cm). The electrolyte solution was deaerated by argon gas bubbling for 30 min. Linear sweep voltammetry were performed by means of a galvanostat/potentiostat (HZ-7000, Hokuto Denko) with scan rate = 20 mV s^{-1}. The amount of O_2 evolved was measured by gas chromatography (GC-2010Plus with BID-detector, Shimadzu) using an Rt-Msieve 5A column (Shimadzu GLC) with helium gas flow rate = 10 mL min^{-1}. Electrochemical impedance spectroscopy (EIS) measurements were carried out in the same EC cell using a frequency response analyzer (HZA-FRA1, Hokuto Denko) built in the galvanostat/potentiostat. The measurements were carried out applying a 10 mV AC sinusoidal signal over the frequency range between 100 mHz and 100 kHz. The series resistance (R) and charge transfer resistance (R_{ct}) were estimated by curve fitting for the Nyquist plots. The overpotential (η) was calculated from eqn (2) by taking the IR drop.

$$\eta = E - I \times R \quad (2)$$

where R is the ohmic resistance determined by the EIS analysis.

Cyclic voltammograms

A three-electrode EC cell was fabricated with the structure of RuO_2//TiO_2 NWA (working electrode), Ag/AgCl (reference electrode)|0.1 M $NaClO_4$ electrolyte solution containing 10 mM $K_3[Fe(CN)_6]$ and 1 mM $K_4[Fe(CN)_6]$||Pt film (counter electrode). The active area of the working electrode was 1 cm^2 (1 cm × 1 cm). The electrolyte solution was deaerated by argon gas bubbling for 30 min. Cyclic voltammograms (CVs) were obtained by means of a galvanostat/potentiostat (HZ-7000, Hokuto Denko) with scan rate = 20 mV s^{-1}.

Results

Electrode preparation and characterization

According to the hydrothermal method previously reported,[30] rutile TiO_2 NWAs were heteroepitaxially grown from fluorine-doped tin oxide (FTO) substrate with the orientation of $(001)_{TiO_2}$//$(001)_{SnO_2}$ (TiO_2 NWA).[31] Then, TiO_2 NWA was immersed into a 67% methanol aqueous solution containing various amounts of $RuCl_3$ and heated at 453 K in a Teflon-lined stainless-steel autoclave for 8 h. The samples prepared by this solvothermal (ST) reaction were calcined at 673 K for 10 h. NWAs with a length of ~3 μm and a square cross-section of ~200 nm × ~200 nm were grown vertically or obliquely with respect to the FTO surface (Fig. 2a). The amount of Ru loaded on TiO_2 NWA was quantified by inductively-coupled plasma spectroscopy to be expressed as that of RuO_2 (x/μg cm^{-2}). The x value of the sample increases with an increase in the content of $RuCl_3$ in the ST-reaction solution to be controlled at $x \leq 43$ (Fig. S1†). High-angle annular dark field (HAADF)-scanning transmission electron microscopy (STEM) measurements were carried out for a piece of the NWs of an ST-sample (x = 18) (Fig. 2b and c). The TiO_2 NW surface is uniformly covered by an ultrathin film containing Ru with a thickness of ~2.5 nm. For comparison, RuO_2 was also loaded on TiO_2 NWA (x = 18) by the conventional impregnation (Im) method.[32] In contrast to the ST-sample, RuO_2 nanoparticles (NPs) with size of ~5 nm were observed on the surfaces of TiO_2 NWA in the Im-sample (Fig. S2†).

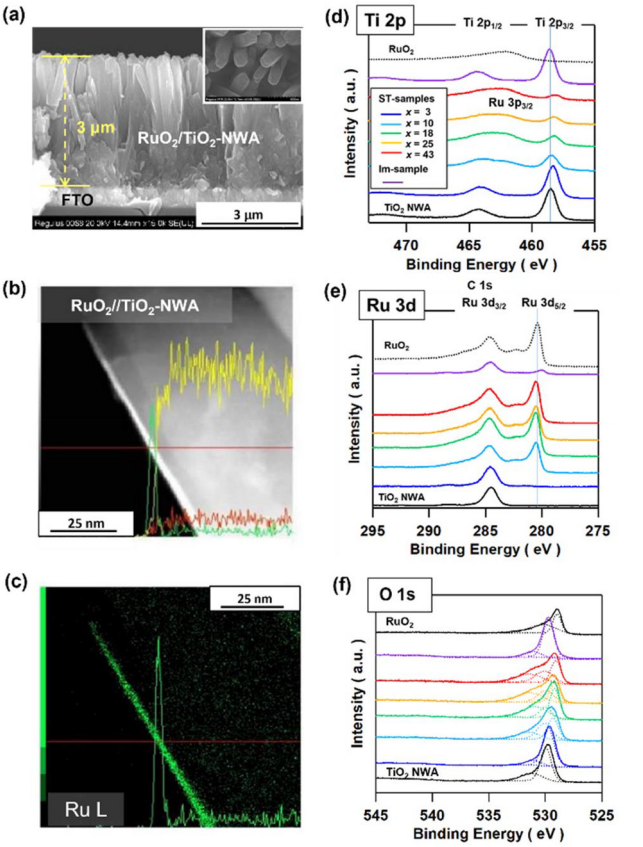

Fig. 2 (a) SEM image of the cross-section of the ST-sample (x = 18). The inset shows the SEM image of the surface (yellow Ti, green Ru, red O). (b and c) HAADF-STEM images of the ST-sample (x = 18) (yellow Ti, green Ru, red O). (d–f) XP spectra of ST-samples (x), and TiO_2 NWA and Im-sample for comparison.

To identify the deposits and examine the electronic state, X-ray photoelectron spectra (XPS) were measured for the samples. In the Ti 2p XPS for an unmodified TiO_2 NWA, two signals are located at binding energy = 458.6 eV and 464.3 eV due to the emission from the Ti $2p_{3/2}$ and Ti $2p_{1/2}$ orbitals of TiO_2 (Fig. 2d).[33] After the ST-reaction, the Ti$2p_{3/2}$ signal rapidly weakens with an increase in x and shifts to a lower binding energy, while a broad signal appears at about 463 eV due to the emission from the Ru $3p_{3/2}$ orbital of RuO_2[34] at $x \geq 10$. A similar redshift in the binding energy of the Ti $2p_{3/2}$ signal was reported previously in the growth of RuO_2 films on TiO_2(110) by physical vapor deposition at 600 K.[35] The authors attributed this result to the formation of a Schottky barrier at the junction by measuring the valence band spectra.

Meanwhile, the Ti $2p_{3/2}$ signal intensities of the Im-sample at $x = 3$ remain almost unchanged compared to that of the unmodified TiO_2 NWA. In the Ru 3d-XP spectra of the ST-samples (Fig. 2e), the emission from the Ru $3d_{5/2}$ orbital is observed at 280.5 eV, which is in agreement with the value reported for the RuO_2(110) surface,[36] and the signal intensifies with an increase in x. In the O 1s spectra (Fig. 2f), TiO_2 and RuO_2 have main signals at 529.8 eV and 529.0 eV due to the emission from the lattice oxygen, respectively, and a broad signal at about 531.5 eV tentatively assigned to the surface OH groups. For the ST samples, the ratio of the RuO_2 signal intensity to TiO_2 signal intensity (I_{RuO_2}/I_{TiO_2}) increases with increasing x in the range of $x \leq 18$ but tends to decrease beyond that (Table S2†). In addition, the O 1s binding energy of the ST-sample gradually shifts to lower energy from the value of TiO_2 to that of RuO_2. On the contrary, the binding energy of the Im-sample is close to the value of TiO_2. These results are consistent with the TEM observation that uniform RuO_2 films are formed on the surface of TiO_2 NWA in the ST-sample with $x \geq 10$, whereas RuO_2 NPs are sparsely precipitated on the surface in the Im-sample. The decrease in the I_{RuO_2}/I_{TiO_2} ratio in the ST-sample at $x > 18$ suggests that if the RuO_2 film is too thick, it may cause degradation of the film quality due to cracks.

Interface analysis

High resolution (HR)-TEM analysis was further performed for an NW of the ST-sample ($x = 18$) to scrutinize the state of junction between RuO_2 and TiO_2 (red square part in Fig. 3a). The TiO_2 NW is a single crystal growing in the [001] direction with the (110) facets on the large-area side walls, as previously reported (Fig. 3b).[31] Interestingly, a uniform film with a thickness of ~2.5 nm is formed on the TiO_2(110) surface, and the d-spacing of 3.03 Å matches with the RuO_2(110) interplanar distance. Also, the surface of TiO_2 is covered with a single-crystal RuO_2 film with a $(110)_{RuO_2}//(110)_{TiO_2}$ orientation (Fig. 3b and Fig. S3†).

Both rutile TiO_2 and RuO_2 belong to the tetragonal crystal system ($P4_2/mnm$), and the lattice constants are a = 4.5933 Å and c = 2.9592 Å for TiO_2 (ICDD no. 00-021-1276) and a = 4.4968 Å and c = 3.1049 Å for RuO_2 (ICDD no. 01-088-0286). There are only small a-axis and c-axis mismatches ($\{(a_{RuO_2} - a_{TiO_2})/a_{TiO_2}\} \times 100$) of −2.1% and ($\{(c_{RuO_2} - c_{TiO_2})/c_{TiO_2}\} \times 100$) of +4.9% between RuO_2 and TiO_2, respectively. A HEPI junction model constructed using the bulk crystal dimensions for each component indicates that a single-crystalline RuO_2 film can be formed on the rutile TiO_2 surface with the $(110)_{RuO_2}//(110)_{TiO_2}$ orientation (Fig. 3c and d). Further, selected area electron diffraction (SAED) was measured for TiO_2 NW covered by the RuO_2 film (red square part in Fig. 3e). A clear spot pattern is observed in the SAED pattern (Fig. 3f), further supporting the conclusion that single-crystal RuO_2 films are formed on the side walls of the single crystal TiO_2 NWA with the orientation. Thus, the formation of the strong interfacial Ru–O–Ti bonds may also contribute to the shift in the Ti $2p_{3/2}$-XPS signal toward lower binding energy (Fig. 2d). The sample with an

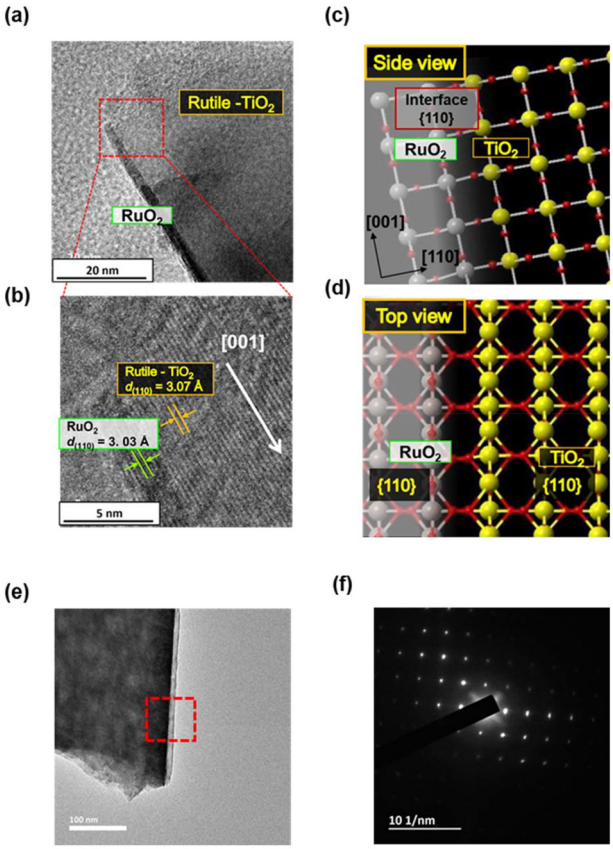

Fig. 3 TEM image (a) and HR-TEM image (b) of RuO_2 (x = 18)-deposited TiO_2 NW. Side view (c) and top view (d) of the interface model between RuO_2 and rutile TiO_2. TEM image (e) and (f) SAED pattern of the sample with at x = 18, respectively.

RuO_2-loading amount of x (μg cm^{-2}) is designated as ST-$RuO_2(x)$//TiO_2 NWA below.

On the other hand, in the Im-sample (x = 18, Fig. S2†), there are some aggregates of RuO_2 NPs, and part of them do not appear to be in direct contact with the TiO_2 NW surface (Im-RuO_2/TiO_2 NWA).

Electrocatalytic activity for OER

The OER polarization curves of TiO_2 NWA, Im-RuO_2(18)/TiO_2 NWA, and ST-$RuO_2(x)$//TiO_2 NWAs were measured in 0.5 M H_2SO_4 electrolyte solution in the dark. Electrode potential (E) was corrected to compensate the effect of solution resistance (R) determined by electrochemical impedance spectroscopy (EIS) measurements (*vide infra*) and expressed with respect to the reversible hydrogen electrode (E–iR, E_{corr} *vs.* RHE) unless otherwise noted. The amount of O_2 evolved over the ST-RuO_2(18)//TiO_2 NWA electrode (n_{O_2}) was quantified by gas chromatography. The n_{O_2} increases linearly with electrolysis time (t_e), confirming that the OER proceeds at a constant rate of 1.86 μmol min^{-1} and a faradaic efficiency of ~100% (Fig. S4†). ST-$RuO_2(x)$//TiO_2 NWAs show much higher activity for OER compared to unmodified TiO_2 NWA and Im-RuO_2/TiO_2 NWA (Fig. 4a and Fig. S5†). The overpotential for OER (η)

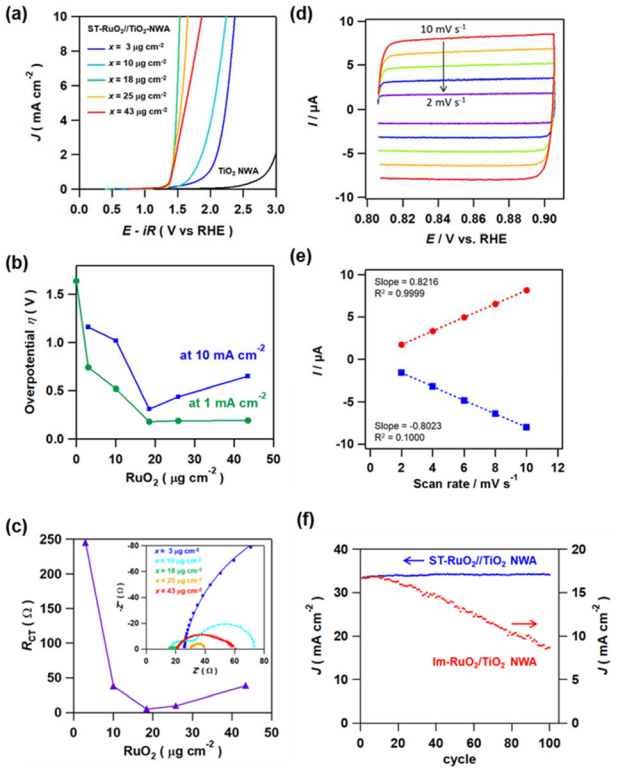

Fig. 4 (a) OER polarization curves of TiO_2 NWA and ST-RuO_2(x)//TiO_2 NWAs in 0.5 M H_2SO_4 electrolyte solution in dark. (b) Overpotential (η) of ST-RuO_2//TiO_2 NWAs for OER as a function of x. (c) Charge transfer resistance obtained by electrochemical impedance analysis for ST-RuO_2(x)//TiO_2 NWAs as a function of x. The inset shows the fitted Nyquist plots. (d) Non-faradaic polarization curves of ST-RuO_2(18)//TiO_2 NWA electrode with varying potential scan rate (v). (e) Plots of current *vs.* scan rate. (f) Stability test for Im-RuO_2/TiO_2 NWA, and ST-RuO_2(18)//TiO_2 NWA. CV curves were measured at a potential scan rate of 20 mV s^{-1}.

at current density = 10 mA cm^{-2} initially decreases with increasing x to reach a minimum at x = 18 and then gradually increases (Fig. 4b). The minimal value of 303 mV is close to the values of 300 mV at x = 300 (ref. 25 and 26) and 320 mV at x = 637 (ref. 27) recently reported for RuO_2.

EIS measurements were performed, and the data was analyzed using an equivalent circuit in which charge transfer resistance (R_{ct}) coupled in parallel with constant phase element (CFE) was connected in series with ohmic resistance (R) (Fig. S6 and Table S3†). In the fitted Nyquist plots for the ST-RuO_2(x)//TiO_2 NWA electrodes (inset in Fig. 4c), the R_{ct} corresponding to the diameter of the semicircle decreases parallelly with an increase in the OER activity to reach a minimum of 4.9 Ω at x = 18 (Fig. 4c).

To gain insights into the origin of the large difference in the electrocatalytic activities between the ST-RuO_2(3)//TiO_2 NWA and ST-RuO_2(18)//TiO_2 NWA electrodes, cyclic voltammograms (CVs) were measured in a 0.1 M $NaClO_4$ electrolyte solution containing 10 mM $K_3[Fe(CN)_6]$ and 1 mM $K_4[Fe(CN)_6]$ degassed by argon bubbling (Fig. S7†). In the unmodified TiO_2 NWA electrode, cathodic current is observed at a potential negative than ~0 V *vs.* standard hydrogen electrode (SHE), but current hardly flows in the potential range from 0 V to 0.8 V since TiO_2 is an n-type semiconductor. In contrast, the ST-RuO_2(18)//TiO_2 NWA electrode affords a couple of redox current peaks in a manner similar to that of the usual metal electrodes at a half-wave potential ($E_{1/2}$) of 0.41 V close to the redox potential of $[Fe(CN)_6]^{3-}$/$[Fe(CN)_6]^{4-}$ (0.36 V *vs.* SHE).[37] In the CV curve of the ST-RuO_2(3)//TiO_2 NWA electrode, weak redox currents are observed. These results also support the conclusion from XPS (Fig. 2d and e) that the surface of TiO_2 NWA and exposed FTO is completely covered by the RuO_2 film in ST-RuO_2(18)//TiO_2 NWA, while the surface of TiO_2 NWA is only partly covered in ST-RuO_2(3)//TiO_2 NWA (Fig. S8†).

Further, non-faradaic current (I) of ST-RuO_2(18)//TiO_2 NWA was measured at 0.81 V ≤ E ≤ 0.91 V under varying potential scan rates (v). The current increases monotonically with an increase in v (Fig. 4d), and the I–v plot provides straight lines (Fig. 4e). From the slope, the electrochemically active surface area (ECSA) was calculated to be 23 using the specific capacitances of C_s = 0.035 mF cm^{-2} in 1 M H_2SO_4.[38] Thus, the high electrocatalytic activity of ST-RuO_2(18)//TiO_2 NWA is ascribable to the uniformity, high-quality, and large actual surface area of the RuO_2 film. TiO_2 NWA is an important semiconductor electrode widely used in the field of photoelectrochemistry, but it is impossible to directly measure the ECSA. Making this possible is a distinctive feature of the present RuO_2 plating technique from an analytical point of view.

To check the stability of the electrodes, CVs were measured at 1.0 V ≤ E ≤ 2.2 V (Fig. 4f). In the Im-RuO_2(18)/TiO_2 NWA electrode, the initial current at E = 2.2 V of 16.9 mA cm^{-2} decreased to 9.0 mA cm^{-2} after 100 cycles (Fig. S9†). On the other hand, in the ST-RuO_2(18)//TiO_2 NWA electrode, the current of 34.0 mA cm^{-2} hardly changed during the cycles (Fig. S9†). Also, in the Ru 3d XP spectra of the ST-RuO_2(18)//TiO_2 NWA electrode, the signal intensity hardly changes after the 100 cycle-electrolysis (Fig. S10†). Further, the HR-TEM image of the ST-RuO_2(18)//TiO_2 NWA electrode after 100-cycle electrolysis shows that a uniform RuO_2 thin film with a thickness of ~2.5 nm is maintained (Fig. S11†).

Discussion

The action mechanism of the electrode is discussed using the schematic (Scheme 1). The present ST-post heating process can create uniform ultrathin single-crystal RuO_2 films on the large area (110) side walls of TiO_2 NWA. The strong bonding between the TiO_2 NWA and the RuO_2 film is caused by the HEPI junction with the $(110)_{RuO_2}$//$(110)_{TiO_2}$ orientation. The loading amount and morphology of RuO_2 on TiO_2 NWA can be controlled by the content of $RuCl_3$ in the reaction solution.

The activity of ST-RuO_2(x)//TiO_2 NWA for EC OER steeply increases with an increase in x to reach a maximum at x = 18, where a uniform RuO_2 film with a thickness of ~2.5 nm is formed on the TiO_2 NWA and the exposed FTO surfaces. The

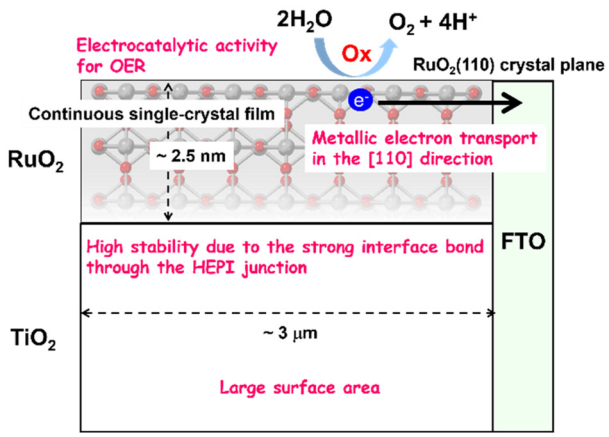

Scheme 1 Action mechanism of the ST-RuO_2(18)//TiO_2 NWA anode for EC OER.

continuous RuO_2 film is in direct contact with FTO, and the Fermi energy of RuO_2 agrees with that of the FTO electrode. The ST-RuO_2(18)//TiO_2 NWA electrode can output significantly higher current than the recently reported RuO_2 electrodes, even though the x value of the former is more than an order of magnitude smaller than the x values of the latter. Consequently, the MSA at E = 1.5 V reaches 341 A g_{cat}^{-1} at only x = 18 (blue circle in Fig. 1). In this system, the SA was also calculated from the values of MSA, x, and ECSA to be 267 μA cm^{-2}, which is much larger than the value of 64.3 μA cm^{-2} reported for RuO_2 (111) surface at 1.53 V in 0.1 M KOH.[39] Thus, the impressive MSA of ST-RuO_2(18)//TiO_2 NWA at x = 18 is ascribable to the uniformity, high-quality, and large surface area of the RuO_2 film working as both a good electrocatalyst for OER and electric conductor. In addition to the high-quality of the RuO_2 film, the strong Ti–O–Ru interfacial chemical bond (Fig. 3c and d) and the large-area interface would contribute to the high stability of the ST-RuO_2(18)//TiO_2 NWA anode under harsh conditions. The trend is observed that the η at 10 mA cm^{-2} and R_{ct} somewhat increases at x > 18. Since the η at 1 mA cm^{-2} is almost constant at 18 ≤ x ≤ 43, the increase in the η at 10 mA cm^{-2} in the range of x above 18 may be incurred by a slight deterioration of the electronic property of RuO_2, as suggested by the O 1s XPS (Table S2†).

Conclusion

The important findings of this study are as follows. (1) By virtue of the crystallographic interface design, single-crystalline RuO_2 films were formed on TiO_2 NWA using a two-step process consisting of the solvothermal reaction and post heating with the loading amount and morphology of RuO_2 controlled by the content of the Ru source ($RuCl_3$). (2) This metal–oxide plating technique made it possible to measure the ECSA of TiO_2 NWA electrodes. (3) The activity of the ST-RuO_2//TiO_2 NWA electrode for EC OER reached a maximum at x = 18, where the whole surface of TiO_2 NWA and the FTO underlayer is covered by a uniform and continuous RuO_2 film with thickness of ~2.5 nm. In addition to the remarkable OER performances with the loading of a slight amount of RuO_2, the high stability renders ST-RuO_2//TiO_2 NWA very promising as a high cost-performance anode for water splitting.

Author contributions

S. N. and M. N. prepared the electrodes, and carried out EC experiments and the analysis, T. S. performed HR-TEM measurements and the analysis, and H. T. and H. S. supervised the experimental work and data analysis.

Data availability

The authors confirm that the data supporting the findings of this study are available within the article and its ESI.†

Conflicts of interest

There are no conflicts to declare.

Acknowledgements

The authors acknowledge K. Miyazaki, R. Kuma, T. Sento, and M. Shima (Nippon Shokubai Co., Ltd) for helpful discussion. This work was financially supported by JSPS KAKENHI Grant-in-Aid for Scientific Research (C) no. 21K05236 and 23K04545, the Futaba Foundation, Nippon Sheet Glass Foundation for Materials Science and Engineering, Sumitomo Foundation, and Kato Foundation for Promotion of Science.

References

1 N. S. Lewis and D. G. Nocera, Powering the planet: chemical challenges in solar energy utilization, *Proc. Natl. Acad. Sci. U. S. A.*, 2006, **103**, 15729–15735.
2 M. W. Kanan and D. G. Nocera, In situ formation of an oxygen-evolving catalyst in natural water containing phosphate and Co^{2+}, *Science*, 2008, **321**, 1072–1075.
3 C. Spöri, J. T. H. Kwan, A. Bonakdarpour, D. P. Wilkinson and P. Strasser, The stability challenges of oxygen evolving catalysts: towards a common fundamental understanding and mitigation of catalyst degradation, *Angew. Chem., Int. Ed.*, 2017, **56**, 5994–6021.
4 I. C. Man, H.-Y. Su, F. Calle-Vallejo, H. A. Hansen, J. I. Martinez, N. G. Inoglu, J. Kitchin, T. F. Jaramillo, J. K. Nørskov and J. Rossmeisl, Universality in oxygen evolution electrocatalysis on oxide surfaces, *ChemCatChem*, 2011, **3**, 1159–1165.

5 H. Over, Chemistry of ruthenium dioxide in heterogeneous catalysis and electrocatalysis: from fundamental to applied research, *Chem. Rev.*, 2012, **112**, 3356–3426.
6 T. Bhowmik, M. K. Kundu and S. Barman, Growth of one-dimensional RuO_2 nanowires on g-carbon nitride: an active and stable bifunctional electrocatalyst for hydrogen and oxygen evolution reactions at all pH values, *ACS Appl. Mater. Interfaces*, 2016, **8**, 28678–28688.
7 T. Audichon, T. W. Nappom, C. Canaff, C. Morais and C. Comminges, IrO_2 coated on RuO_2 as efficient and stable electroactive nanocatalysts for electrochemical water splitting, *J. Phys. Chem. C*, 2016, **120**, 2562–2573.
8 S. Chen, H. Huang, P. Jiang, K. Yang, J. Diao, S. Gong, S. Liu, M. Huang, H. Wang and Q. Chen, Mn-doped RuO_2 nanocrystals as highly active electrocatalysts for enhanced oxygen evolution in acidic media, *ACS Catal.*, 2020, **10**, 1152–1160.
9 L. Zhang, H. Jang, H. Liu, M. G. Kim, D. Yang, S. Liu, X. Liu and J. Cho, Sodium-decorated amorphous/crystalline RuO_2 with rich oxygen vacancies: a robust pH-universal oxygen evolution electrocatalyst, *Angew. Chem., Int. Ed.*, 2021, **60**, 18821–18829.
10 Y. Wen, C. Liu, R. Huang, H. Zhang, X. Li, F. P. G. de Arguer, Z. Liu, Y. Li and B. Zhang, Introducing Brønsted acid sites to accelerate the bridging-oxygen-assisted deprotonation in acidic water oxidation, *Nat. Commun.*, 2022, **13**, 4871.
11 S.-C. Sun, H. Jiang, Z.-Y. Chen, Q. Chen, M.-Y. Ma, L. Zhen, B. Song and C.-Y. Xu, Bifunctional WC-supported RuO_2 nanoparticles for robust water splitting in acidic media, *Angew. Chem., Int. Ed.*, 2022, **61**, e202202519.
12 K. Wang, Y. Wang, B. Yang, Z. Li, X. Qin, Q. Zhang, M. Lei, G. Wu and Y. Hou, Highly active ruthenium sites stabilized by modulating electron-feeding for sustainable acidic oxygen-evolution electrocatalysis, *Energy Environ. Sci.*, 2022, **15**, 2356–2365.
13 Y. Qin, T. Yu, S. Deng, X.-Y. Zhou, D. Lin, Q. Zhang, Z. Jin, D. Zhang, Y.-B. He, H.-J. Qiu, L. He, F. Kang, K. Li and T.-Y. Zhang, RuO_2 electronic structure and lattice strain dual engineering for enhanced acidic oxygen evolution reaction performance, *Nat. Commun.*, 2022, **13**, 3784.
14 J. Zhang, R. Lin, Y. Zhao, H. Wang, S. Liu and X. Cai, Modulation for RuO_2/TiO_2 via simple synthesis to enhance the acidic oxygen evolution reaction, *ACS Sustainable Chem. Eng.*, 2023, **11**, 9489–9497.
15 T. Feng, J. Yu, D. Yue, H. Song, S. Tao, G. I. N. Waterhouse, S. Lu and B. Yang, Defect-rich ruthenium dioxide electrocatalyst enabled by electronic reservoir effect of carbonized polymer dot for remarkable pH-universal oxygen evolution, *Appl. Catal., B*, 2023, **328**, 122546.
16 Y. Wang, R. Yang, Y. Ding, B. Zhang, H. Li, B. Bai, M. Li, Y. Cui, J. Xiao and Z.-S. Wu, Unraveling oxygen vacancy site mechanism of Rh-doped RuO_2 catalyst for long-lasting acidic water oxidation, *Nat. Commun.*, 2023, **14**, 1412.
17 Y. Liu, T. Duan, L. Xu, X. Gao, L. Xue, Y. Xin, L. Ma, G. Huang and T. Liu, Electrocatalyst of RuO_2 decorating TiO_2 nanowire arrays for acidic oxygen evolution, *Int. J. Hydrogen Energy*, 2023, **48**, 10737–10754.
18 J. Wang, C. Cheng, Q. Yuan, H. Yang, F. Meng, Q. Zhang, L. Gu, J. Cao, L. Li, S.-C. Haw, Q. Shao, L. Zhang, T. Cheng, F. Jiao and X. Huang, Exceptionally active and stable RuO_2 with interstitial carbon for water oxidation in acid, *Chem*, 2022, **8**, 1673–1687.
19 C. Liu, Y. Jiang, T. Wang, Q. Li and Y. Liu, Nano Si-doped ruthenium oxide particles from caged precursors for high-performance acidic oxygen evolution, *Adv. Sci.*, 2023, **10**, 2207429.
20 J. Wang, H. Yang, F. Li, L. Li, J. Wu, S. Liu, T. Cheng, Y. Xu, Q. Shao and X. Huang, Single-site Pt-doped RuO_2 hollow nanospheres with interstitial C for high-performance acidic overall water splitting, *Sci. Adv.*, 2022, **8**, eabl9271.
21 R. Gong, B. Liu, X. Wang, S. Du, Y. Xie, W. Jia, X. Bian, Z. Chen and Z. Ren, Electronic structure modulation induced by cobalt-doping and lattice-contracting on armor-like ruthenium oxide drives pH-universal oxygen evolution, *Small*, 2023, **19**, 2204889.
22 Y. Lin, Z. Tian, L. Zhang, J. Ma, Z. Jiang, B. J. Deibert, R. Ge and L. Chen, Chromium-ruthenium oxide solid solution electrocatalyst for highly efficient oxygen evolution reaction in acidic media, *Nat. Commun.*, 2019, **10**, 162.
23 Y. Wen, P. Chen, L. Wang, S. Li, Z. Wang, J. Abed, X. Mao, Y. Min, C. T. Dinh, R. Hang, L. Zhang, L. Wang, L. Wang, R. J. Nielsen, H. Li, T. Zhuang, C. Ke, O. Voznyy, Y. Hu, Y. Li, W. A. Goddard III, B. Zhang, H. Peng and E. H. Sargent, Stabilizing highly active Ru sites by suppressing lattice oxygen participation in acidic water oxidation, *J. Am. Chem. Soc.*, 2021, **143**, 6482–6490.
24 C. A. Grimes, O. K. Varghese and S. Ranjan, *Light, Water, Hydrogen: The solar generation of hydrogen by water photoelectrolysis*, Springer, New York, 2008.
25 S. Wang, G. Liu and L. Wang, Crystal facet engineering of photoelectrodes for photoelectrochemical water splitting, *Chem. Rev.*, 2019, **119**, 5192–5247.
26 V. Andrei, I. Roh and P. Yang, Nanowire photochemical diodes for artificial photosynthesis, *Sci. Adv.*, 2023, **9**, eade9044.
27 W. D. Ryden, A. W. Lawson and C. C. Sartain, Electrical transport jproperties of IrO_2 and RuO_2, *Phys. Rev. B: Condens. Matter Mater. Phys.*, 1970, **4**, 1494–1500.
28 W. Yuan, B. Zhu, K. Fang, X.-Y. Li, T. W. Hansen, Y. Ou, H. Yang, J. B. Wagner, Y. Gao, Y. Wang and Z. Zhang, In situ manipulation of the active Au-TiO_2 interface with atomic precision during CO oxidation, *Science*, 2021, **371**, 517–521.
29 H. Tada, S. Naya and M. Fujishima, Nanohybrid crystals with heteroepitaxial junctions for solar-to-chemical transformations, *J. Phys. Chem. C*, 2020, **124**, 25657–25666.
30 B. Liu and E. S. Aydil, Growth of oriented single-crystalline rutile TiO_2 nanorods on transparent conducting substrates for dye-sensitized solar cells, *J. Am. Chem. Soc.*, 2009, **131**, 3985–3990.

31 A. Akita and H. Tada, Synthesis of 1D-anisotropic particles consisting of TiO_2 nanorod and SnO_2 with heteroepitaxial junction and the self-assembling to 3D-microsphere, *Langmuir*, 2019, **35**, 17096–17102.
32 L. Manjakkal, K. Cvejin, J. Kulawik, K. Zaraska, D. Szwagierczak and G. Stojanovic, Sensing mechanism of RuO_2–SnO_2 Thick film pH sensors studied by potentiometric method and electrochemical impedance spectroscopy, *J. Electroanal. Chem.*, 2015, **759**, 82–90.
33 B. Feng, J. Y. Chen, S. K. Qi, L. He, J. Z. Zhao and X. D. Zhang, Characterization of surface oxide films on titanium and bioactivity, *J. Mater. Sci.*, 2002, **13**, 457–464.
34 N. Luo, H. Cai, X. Li, M. Guo, C. Wang, X. Wang, P. Hu, Z. Cheng and J. Xu, Non-crystal-RuO_x/crystalline-ZnO composites: controllable synthesis and high-performance toxic gas sensors, *J. Mater. Chem. A*, 2022, **10**, 15136–15145.
35 Y. He, D. Langsdorf, L. Li and H. Over, Versatile model system for studying processes ranging from heterogeneous to photocatalysis: Epitaxial RuO_2(110) on TiO_2(110), *J. Phys. Chem. C*, 2015, **119**, 2692–2702.
36 H. Over, A. P. Seitsonen, E. Lundgren, M. Smedh and J. N. Andersen, On the origin of the Ru-$3d_{5/2}$ satellite feature from RuO_2(110), *Surf. Sci.*, 2002, **504**, L196–L200.
37 *Denki Kagaku Binran*, Electrochemical Society of Japan: Maruzen, Tokyo, 5th edn, 2000.
38 C. C. L. McCrory, S. Jung, J. C. Peters and T. F. Jaramillo, Benchmarking heterogeneous electrocatalysts for the oxygen evolution reaction, *J. Am. Chem. Soc.*, 2013, **135**, 16977–16987.
39 K. A. Stoerzinger, O. Diaz-Morales, M. Kolb, R. R. Rao, R. Frydendal, L. Qiao, X. R. Wang, N. B. Halck, J. Rossmeisl, H. A. Hansen, T. Vegge, I. E. L. Stephens, M. T. M. Koper and S.-H. Yang, Orientation-dependent oxygen evolution on RuO_2 without lattice exchange, *ACS Energy Lett.*, 2017, **2**, 876–881.